Published in final edited form as:
Phys Med Biol. 2013 July 21; 58(14): 4749–4761. doi:10.1088/0031-9155/58/14/4749.

Combined Ultrasound and MR Imaging to Guide Focused Ultrasound Therapies in the Brain

Costas D. Arvanitis[1], **Margaret S. Livingstone**[2], and **Nathan McDannold**[1]

[1]Department of Radiology, Brigham and Women's Hospital, Harvard Medical School, 221 Longwood Avenue, Boston, MA 02115, Massachusetts, USA

[2]Department of Neurobiology, Harvard Medical School, 220 Longwood Avenue, Boston, MA 02115, Massachusetts, USA

Abstract

Purpose—Several emerging therapies with potential for use in the brain harness effects produced by acoustic cavitation – the interaction between ultrasound and microbubbles either generated during sonication or introduced into the vasculature. Systems developed for transcranial MRI-guided focused ultrasound (MRgFUS) thermal ablation can enable their clinical translation, but methods for real-time monitoring and control are currently lacking. Acoustic emissions produced during sonication can provide information about the location, strength, and type of the microbubble oscillations within the ultrasound field, and they can be mapped in real-time using passive imaging approaches. Here, we tested whether such mapping can be achieved transcranially within a clinical brain MRgFUS system.

Materials and Methods—We integrated an ultrasound imaging array into the hemisphere transducer of the MRgFUS device. Passive cavitation maps were obtained during sonications combined with a circulating microbubble agent at 20 targets in the cingulate cortex in three macaques. The maps were compared with MRI-evident tissue effects.

Results—The system successfully mapped microbubble activity during both stable and inertial cavitation, which was correlated with MRI-evident transient blood-brain barrier disruption and vascular damage, respectively. The location of this activity was coincident with the resulting tissue changes within the expected resolution limits of the system.

Conclusion—While preliminary, these data clearly demonstrate, for the first time, that is possible to construct maps of stable and inertial cavitation transcranially, in a large animal model, and under clinically relevant conditions. Further, these results suggest that this hybrid ultrasound/MRI approach can provide comprehensive guidance for targeted drug delivery via blood-brain barrier disruption and other emerging ultrasound treatments, facilitating their clinical translation. We anticipate it will also prove to be an important research tool that will further the development of a broad range of microbubble-enhanced therapies.

1. Introduction

Transcranial MRI-guided FUS (MRgFUS) is an enabling technology that can have a broad clinical impact, as FUS can induce a number of bioeffects in addition to heating (Martin *et al.*, 2009; McDannold *et al.*, 2010) that can be used for different therapeutic applications. Many of these applications utilize acoustic cavitation – the interactions between ultrasound and microbubbles that are either generated acoustically at the focus or introduced into the

Corresponding author: Costas D. Arvanitis, Ph.D., Address: 221 Longwood Avenue, Room 514a, Boston, MA 02115, Phone: 617 525 6860, FAX: 617 525 7450, cda@bwh.harvard.edu.

vasculature. For example, when low-intensity ultrasound bursts are applied in the presence of a circulating microbubble ultrasound contrast agent, a transient disruption of the blood-brain barrier (BBB) is induced, enabling targeted delivery of pharmaceuticals that are otherwise impermeable to the brain (Hynynen *et al.*, 2001). While MRI is excellent for the planning and assessment for this and other microbubble-mediated FUS procedures, current methods cannot monitor cavitation activity, which occurs over short timescales – milliseconds or microseconds.

Acoustic cavitation is an inherently nonlinear phenomenon due to asymmetric expansion and contraction that occurs when a microbubble oscillates in an ultrasound field. It can be divided into two regimes: stable and inertial. Stable cavitation refers to volumetric, stable microbubble oscillations within the ultrasound field. Inertial cavitation occurs at higher acoustic pressure amplitudes, where the microbubbles grow to the point where the inertia of the surrounding medium causes a sudden collapse of the microbubble. Stably-oscillating microbubbles can exert forces and shear stress in the surrounding medium that can produce significant bioeffects (Rooney, 1972; Marmottant and Hilgenfeldt, 2003). This type of oscillation, known as the “breathing mode”, has been associated with strong harmonic, and in some cases, ultraharmonic emissions. Such emissions have been proposed to control FUS-induced BBB disruption (Arvanitis *et al.*, 2012; McDannold *et al.*, 2006a; O'Reilly and Hynynen, 2012). Broadband emissions indicate the presence of inertial cavitation, which *in vivo* has been associated with vessel damage (McDannold *et al.*, 2006a; Tung *et al.*, 2010; Arvanitis *et al.*, 2012). For therapies that utilize inertial cavitation, broadband emissions could be used to control the procedure. In other applications, such as BBB disruption and thermal ablation, inertial cavitation is not necessarily desired, broadband emissions would be a signature to reduce the exposure level. Assessment of acoustic cavitation would be an effective means to elucidate the mechanism(s) upon which microbubbles are interacting with biological media. It can provide important information for the preclinical development of these FUS technologies and ultimately a real-time implementation will be needed for their clinical translation.

Currently, the only clinically-relevant method to monitor cavitation activity with high sensitivity and specificity, and at the same time provide information about the mode and strength of the oscillations in real-time, is with acoustic methods – in particular with passive cavitation mapping (Norton and Won, 2000; Gyongy and Coussios, 2010b; Haworth *et al.*, 2012; O'Reilly *et al.*, 2010). This technique uses the FUS device as a source and an array of receivers to passively record and reconstruct the acoustic field. It relies on the fact that an inherent characteristic of oscillating bubbles is the formation of diverging pressure waves at frequencies different than the FUS device (i.e. harmonics, etc.). When multiple acoustic receivers record these waves simultaneously, the sources of the emissions can be estimated through back-propagation to different image coordinates to reconstruct two- or three-dimensional maps of the cavitation activity. The image amplitude reflects the intensity of the acoustic emissions integrated across the array elements whereas the spectral content of the ultrasound RF data reflects the type of the microbubble oscillations. This information can ensure that cavitation is occurring at the targeted location and that the focal intensity is at a level that produces only the desired effect. The images can capture activity occurring over very short timescales (as short as a few microseconds), and they can be obtained at a frame rate that provides real-time control over microbubble-enhanced FUS procedures in the brain.

Integrating a passive cavitation imaging system into an MRgFUS device for brain applications faces several technical challenges due to the presence of the skull (with its high attenuation and acoustic impedance), interference from the MRI system, and the challenging geometry of the hemisphere transducer design used for transcranial sonication (Martin *et al.*, 2009; McDannold *et al.*, 2010). In the present study, we integrated an ultrasound imaging

system operating in a passive mode with a clinical MRgFUS device in order to transcranially map, for the first time, microbubble activity in the brain. The integrated system was tested during FUS-induced BBB disruption produced at discrete targets in nonhuman primates. We examined a range of exposure levels to assess the ability of the device to map both stable and inertial cavitation signals, which we then correlated with post-FUS MRI.

2. Materials and Methods

Experimental Apparatus

A clinical MRgFUS system (ExAblate 4000 low frequency, InSightec), which was developed for high-intensity sonications for transcranial thermal ablation in the brain (Martin *et al.*, 2009), was modified to provide low-power sonications for BBB disruption (Arvanitis *et al.*, 2012; McDannold *et al.*, 2012). This system has a phased array transducer with 1024 elements arranged in a 30 cm diameter hemisphere and operates at a central frequency of 220 kHz. It was driven in burst mode via a gating signal provided by an arbitrary waveform generator (model 396, Fluke). It was integrated with a clinical 3T MRI unit (GE Healthcare). For this work, the hemisphere transducer was oriented 90° from its normal clinical use so that it could be simply filled with degassed water like a bowl. Imaging was performed using a 15 cm surface coil with the animal placed supine on the MRI scanner table with its head partially submerged in water (Fig. 1). The animal's head was tilted back so that the focal plane of the MRgFUS device, which in this configuration was parallel to the water surface, corresponded to an approximately axial plane in the brain. FUS beam aberration correction (Clement and Hynynen, 2002), which is needed to compensate for beam distortions in a human skull, was not necessary with the thinner primate skull (McDannold *et al.*, 2012). Prior characterization of the ultrasound field in water and after transmission through an *ex vivo* monkey skull found that an acoustic power level of 1 W with this device produces an estimated peak negative pressure amplitude in the brain of approximately 223 kPa (Arvanitis *et al.*, 2012).

The ultrasound imaging probe (L382, Acuson) used for passive cavitation imaging was a 128-element (82 mm) linear array with a 3.21 MHz central frequency and a bandwidth of approximately 75%. It was incorporated into the therapeutic MRgFUS phased array with an acoustic mirror (a 6 mm thick brass plate) placed at 45 degrees with respect to the face of the imaging array. Brass was chosen to minimize image artifacts at the MR images. This reflector enabled the collection of axial ultrasound images of the monkey brain (Fig. 1). The imaging array and reflector were mounted so that the ultrasound imaging plane was at a depth a within a few millimeters of the geometric focus of the MRgFUS device. This plane and the animal position were also selected to be at a depth where the cingulate cortex (see below) was included in the ultrasound imaging. The focal point of the MRgFUS device was steered electronically to different targets in the ultrasound imaging plane using its phased array.

The ultrasound imaging engine (Verasonics) was triggered along with the MRgFUS device using an external trigger from arbitrary waveform generator (Fluke) and was programmed in Matlab (Mathworks) to operate in passive mode. The ultrasonic RF data from 64 elements of the imaging array were recorded synchronously at a sampling rate of 12.84 MHz. Only half of the elements (every other element) were used since the imaging engine could only synchronously read data from 64 channels. Sonications were delivered as a series of 10 ms bursts (see below); the first 180 μs of ultrasonic RF data were recorded for each burst. Forty datasets were recorded for each 50s sonication. Power spectra were displayed in real-time on the computer that controlled the system during sonication; cavitation maps were generated offline on the same computer. The ultrasonic RF data were filtered with a 300 kHz high-pass

Butterworth filter in software in order to remove the signal from the fundamental frequency of the MRgFUS transducer (220 kHz).

The acoustic emissions were also recorded with two MRI-compatible piezoelectric transducers using a separate acoustic emissions monitoring system. The ability of this system, which utilized narrow-band receivers with maximal sensitivity at 620 ± 10 kHz, was demonstrated previously in experiments in nonhuman primates to control the exposure level during BBB disruption (Arvanitis *et al.*, 2012). We used this system, which is capable of transcranially detecting broadband and harmonic emissions, to confirm that the ultrasound imaging probe was recording the same spectral content.

Cavitation mapping

The coherent acoustic emissions recorded by the linear imaging array were summed and back-propagated to form maps (Gyongy and Coussios, 2010b; Norton *et al.*, 2006) proportional to the strength of the emissions produced by the microbubble oscillations. In particular, the wave emitted from each bubble can be modeled as being emitted by a point source $s(r,t)$ originating from position $r(x, y, z)$. By making some simple assumptions, we can locate this point source using the signals recorded at the locations r_n of the N transducer elements. Assuming a constant sound speed c between the bubble and the transducer, the location of the point source can be estimated by coherently summing the recorded acoustic emissions $u(r_n,t$ in (r,t) space, with $t=\frac{|r-r_n|}{c}$. Then, reconstruction of the point source $s(r)=\sum_{i=1}^{N}|r-r_n|\cdot u(r_n,|r-r_n|/c)$ is performed by back-propagating the recorded wavefront to multiple point source coordinates and summing over the array's elements. The $|r-r_n|$ term describes geometric wavefront loss. For the linear array used in this study, the 3-dimensional vectors r are converted to image coordinates x (transverse) and z (axial) $\left(|r-r_n|=\sqrt{(x-x_n)^2+z^2}\right)$ (y=0). The relative point source intensity $I(r) = |s(r)|^2$, after subtracting incoherent background noise (i.e. the DC component) (Norton *et al.*, 2006) is given by:

$$I(r)=\left|\sum_{i=1}^{N}|r-r_n|\cdot\overline{u}\left(r_n,\frac{|r-r_n|}{c}\right)\right|^2-\sum_{i=1}^{N}\left||r-r_n|\cdot\overline{u}\left(r_n,\frac{|r-r_n|}{c}\right)\right|^2$$

This back-propagation algorithm requires knowledge of the speed of sound of the media between each point in the image and the transducer (Gyongy and Coussios, 2010b). For points in the brain, this was estimated by the linear combination of the thicknesses and sound speeds in the water (95 mm, 1480 m/sec at 19°C), brain tissue (31.5 mm, 1541 m/sec), and bone (3.5 mm, 3080 m/sec), which resulted in an average speed of sound of 1537 m/sec (Del Grosso and Mader, 1972; Fry and Barger, 1978). The brain and water path thicknesses were measured from the MR images, whereas the bone thickness was measured from head scans obtained with a portable CT scanner (Ceretom). It is important to note that due the small fraction of the bone with respect to beam path, relatively small variations in the speed of sound of the skull are not expected to substantially affect the apparent location of the cavitation activity. Maps were normalized relative to data obtained few minutes earlier without the microbubble agent to remove harmonics or other nonlinear terms present during sonication without the ultrasound contrast agent. The resulting images were expressed in dB.

The axial×transverse field of view was set to 100×80 mm, which included the entire monkey head in the image. With the 8.2 cm aperture of the ultrasound imaging probe, the 13 cm distance from the focal targets in the brain (see below) and a 3.21 MHz central frequency, the theoretical axial and transverse resolution of the cavitation maps is expected to be 0.6 and 7.7 mm, respectively (Gyongy and Coussios, 2010a). As the device was also expected to record higher-frequency content (and for visualization purposes), we reconstructed the images at a higher resolution (axial×transverse pixel dimensions: 0.5×0.5 mm). Therefore, due to the geometry used, the cavitation maps will appear elongated along the axial direction of the array, which is perpendicular to the FUS-beam axial direction.

The high-pass filtered RF data that were recorded from the array were used to construct the cavitation maps. In this article, stable cavitation map refers to absence of broadband emissions from the RF data recorded by the array. The absence of broadband emissions was also confirmed by the single element passive cavitation detection system that was operated in parallel to the passive mapping. This system was able to capture the entire 10 ms RF waveform and determine the spectral signature of the emissions from the entire sonication, as described previously (Arvanitis *et al.*, 2012). Thus, the reports below of inertial cavitation in the passive maps refer to cases where obvious broadband emissions were evident in the spectra obtained by either system. No comb filtering or specific spectral band has been used to form the cavitation maps in the data presented here. Therefore, in the presence of broadband emissions all possible types of oscillation, including inertial, might be included.

MR Imaging and Analysis

Fiducial markers (MR-Spots, Beekley Medical) visible in both MRI and B-mode ultrasound imaging were used before the animal experiments to register the two imaging modalities. the registration accuracy was limited by the size of fiducial markers (<1.5mm) (Arvanitis and McDannold, 2011). Standard T1-, T2- and T2*-weighted imaging sequences were used to select the brain targets and to evaluate the sonication effects (see Table 1 for scan parameters) (Hynynen *et al.*, 2001). BBB disruption was assessed in T1-weighted imaging via the detection of signal enhancement after intravenous administration of the MRI contrast agent Gd-DTPA (Magnevist, Berlex) at a dose of 0.1 mmol/kg. T2*-weighted MRI was used to detect petechiae that occur when inertial cavitation is produced.

Animals

All experiments were done in accordance with procedures approved by the Harvard University Institutional Animal Care and Use Committee. The animals were anesthetized during all the procedures and were constantly monitored throughout and after recovery. No pain or suffering was evident as a result of the procedures. Monkeys were housed, fed, watered, socially housed, and provided with environmental enrichment according to USDA, OLAW, and AAALAC regulations. The first monkey tested was an adult female macaca mulatta (weight: 6 kg); the other two were juvenile male macaca nemistrina (weight: 4.5–6 kg). Each animal was anesthetized with ketamine (15 mg/kg/h i.m.) and xylazine (0.5 mg/kg/h i.m.), or with ketamine (4 mg/kg/h) and dexmeditomidine (0.01–0.02 mg/kg/h i.m.) and intubated. The head was shaved, and a catheter was placed in a leg vein to inject the ultrasound and MRI contrast agents. Heart rate, blood oxygenation levels, and rectal temperature were monitored during the experiments. Body temperature was maintained with a heated water blanket.

Experimental Procedure

The sonications consisted of 10 ms bursts applied at a pulse repetition frequency of 1 Hz. Two 50 s sonications were delivered in sequence with a delay between sonications of ~5 s. These parameters were selected to be similar to previous work (McDannold *et al.*, 2012)

with this device. In each animal, four targets were sonicated the cingulate cortex, two in each hemisphere. This brain structure was selected because it is an anatomically large and homogeneous gray matter target that was aligned with the axial MRI planes and the ultrasound imaging plane. Each sonication was combined with the microbubble ultrasound contrast agent Definity (Lantheus Medical Imaging), which was infused over the entire sonication via an MRI-compatible infusion pump (Spectra Solaris EP, Medrad,). The microbubble agent was diluted in 5 ml sterile phosphate-buffered saline and infused at a variable rate (1 ml at 0.1ml/s for 10 s and 2 ml at 0.02 ml/s for 100 s). A dose of 40 μl/kg of Definity was used for each target (four times the recommended clinical dose for ultrasound imaging). This dose was chosen to maximize the strength of the emissions (Arvanitis *et al.*, 2012) while remaining close to the clinical dose.

The acoustic power level varied among the different animals and targets. It was set initially to achieve BBB disruption without inertial cavitation using feedback from the acoustic emissions data, as described previously (Arvanitis *et al.*, 2012). At the subsequent sonications and targets, we then explored different acoustic power levels, including those slightly above the inertial cavitation threshold (where minor vessel damage is expected). Overall, 20 targets were sonicated over five experiments in the three monkeys (two sessions with the first two monkeys; one with the third). The acoustic power level ranged from 0.5–2.2 W, which yielded an estimated pressure amplitude in the brain 190–330 kPa (Table 2) (Arvanitis *et al.*, 2012).

After the experiments, we investigated if the location of the cavitation maps was colocalized with the site of the BBB disruption in MRI, and whether the data were consistent with prior work relating the acoustic emissions' spectral content to BBB disruption and tissue damage (Arvanitis *et al.*, 2012). The location of the cavitation activity was determined automatically by finding the pixel with peak image intensity in each cavitation map. The location of the BBB disruption was found manually by selecting the center of the MR enhancing region. Each targeted location was classified as having BBB disruption only or BBB disruption and tissue damage using T2*-weighted imaging, which is hypointense when significant red blood cell extravasation (petechiae) occur (McDannold *et al.*, 2012).

3. Results

The introduction of the ultrasound imaging probe for passive cavitation mapping into the MRgFUS system, along with a brass reflector to direct the imaging plane into the head, did not significantly affect either the MR image quality or the ability of the MRgFUS device to produce localized BBB disruption. Typical examples of images obtained for treatment planning and to visualize the resulting BBB disruption are shown in Fig. 1. The probe was capable of transcranially mapping cavitation activity in the macaque brain, both with and without inertial cavitation (Fig. 2).

Representative cavitation maps are shown in Fig. 2A. They were obtained in the focal plane of the MRgFUS device, where the focus has a circular profile and were formed using the entire bandwidth of the ultrasound imaging array. Due to differences in resolution in the axial and transverse directions of the array, the region with apparent cavitation activity appeared elongated in the axial direction. The spectral content of the emissions (Fig. 2B) affected the size of the region with detected cavitation activity. It appeared to be more localized when broadband and high frequency harmonic emissions were observed (Fig. 2C), which would be expected due to the higher frequency content of the acoustic spectra (Gyongy and Coussios, 2010a). Maps were generated for each transmitted ultrasound burst, which allowed detection of when the microbubbles reached the focal area of the FUS transducer (Fig. 2D). Information (the presence or lack of broadband emissions; arrival of

microbubbles to the focal zone) obtained from singleelement receiver transducers characterized previously with this MRgFUS system (Arvanitis *et al.*, 2012) agreed with the information obtained from the ultrasound RF data that were collected from the imaging probe.

Fusion of the cavitation maps with post-sonication MRI (Fig. 3A) showed that the microbubble activity was confined to the targeted area, and that the peak cavitation activity overlapped with the location of the MRI contrast agent extravasation resulting from the BBB disruption. Hypointense spots in T2*-weighted imaging, which are produced by minor vascular damage induced by inertial cavitation, were found when broadband emissions were observed (Fig. 3B). These spots were smaller than the corresponding regions of BBB disruption, perhaps another explanation why the profiles were more localized when broadband emissions were observed (Fig. 2C),

Overall, 40 passive cavitation maps were obtained during each sonication. In every case, localized activity was evident in at least one of these maps. Fig. 4A shows additional examples from the three animals. Except for one case where the monkey's head shifted during sonication, the areas with strong activity in the passive cavitation maps always included the spot where BBB disruption was evident (i.e. the two agreed within their resolution limits). When the signal in the cavitation maps was greater than 1.75 dB (the estimated noise floor of the mapping), the mean distance between the locations of the maximum pixel in the cavitation maps and the MRI contrast enhancement was 0.0 ± 7.5 and 0.3 ± 1.0 mm in the axial and transverse directions of the ultrasound imaging, respectively (Fig. 4B).

4. Discussion

The ability to localize and characterize cavitation activity is promising for advancing BBB disruption and other microbubble-enhanced procedures since, if they are to reach clinical use, methods need to be established to monitor and control the sonications. Such control is critical in the brain, where mistargeting or overexposure could result in serious side effects. Introducing the imaging probe did not appear to impact the performance of the FUS device or the MRI acquisition for the pulse sequences used; the size of the focal effects produced and the imaging quality were consistent with prior work (McDannold *et al.*, 2012).

Several modifications to the method can improve upon these results. For example, using a lower frequency imaging probe will improve sensitivity to lower frequency emissions that could be more appropriate for recording through a thicker human skull. To account for the resolution reduction due to using a lower frequency, one could increase the aperture of the imaging probe or add a second probe pointed in a perpendicular direction. Assessment of skull-induced beam aberration, as is done now for the transmitted FUS beam for patient treatments (Clement and Hynynen, 2002), might improve localization accuracy. While passive imaging will only need to consider one passage through the skull (unlike standard transmit/receive methods), such aberration should be taken into account. Further, stochastic effects, such as the speckle-like interference pattern associated with the emissions from many bubbles, may also influence the apparent strength and location of the cavitation activity. One may be able to use microbubble oscillation models to correct for these effects. If one can take this and the skull-induced effects into account, the strength of the emissions at each point can be estimated and potentially related to the resulting FUS-induced effects – the strength of the BBB disruption for example (Arvanitis *et al.*, 2012). Ultimately, one could redesign the MRgFUS device with passive imaging in mind, with receivers embedded throughout the hemisphere transducer to create three-dimensional cavitation maps (O'Reilly *et al.*, 2010).

These experiments were performed in the context of FUS-induced BBB disruption, where one aims to ensure that only stable cavitation occurs at the focal region. This passive imaging system was capable of mapping both harmonic-only and broadband emissions and thus appears, with some modification, to be adequate for integration into a closed-loop controller for this procedure. We anticipate that it can also provide important information to guide other microbubble-enhanced applications, such as microbubble-enhanced mechanical or thermal ablation (McDannold *et al.*, 2006b), sonothrombolysis (Meairs *et al.*, 2012), tissue erosion (Parsons *et al.*, 2006), delivery of genes or viruses (Greenleaf *et al.*, 1998; Bazan-Peregrino *et al.*, 2012) or radiosensitization (Czarnota *et al.*, 2012). When combined with MRI, with its superior anatomical imaging compared to other modalities and its ability to map temperature changes, a comprehensive system to plan, monitor, and evaluate the broad range of FUS applications becomes possible.

Acknowledgments

This work was supported by National Institutes of Health award numbers R25CA089017, P41EB015898, P41RR019703, and RC2NS069413. The focused ultrasound system was supplied by InSightec. We are grateful to Greg Clement for letting us use the research ultrasound imaging system for this work.

References

Arvanitis CD, McDannold N. Simultaneous temperature and cavitation activity mapping with a transcranial MR-guided focused ultrasound system. Proc. IEEE International Ultrasonics Sumposium. 2011:128–131.

Arvanitis CD, Vykhodtseva N, Livingstone MS, McDannold N. Controlled Ultrasound-Induced Blood-Brain Barrier Disruption Using Passive Acoustic Emissions Monitoring. PLoS ONE. 2012; 24:9.

Bazan-Peregrino M, Arvanitis CD, Rifai B, Seymour LW, Coussios CC. Ultrasound-induced cavitation enhances the delivery and therapeutic efficacy of an oncolytic virus in an in vitro model. J Control Release. 2012; 157:235–242. [PubMed: 21982902]

Clement GT, Hynynen K. A non-invasive method for focusing ultrasound through the human skull. Physics in medicine and biology. 2002; 47:1219–1236. [PubMed: 12030552]

Czarnota GJ, Karshafian R, Burns PN, Wong S, Al Mahrouki A, Lee JW, Caissie A, Tran W, Kim C, Furukawa M, Wong E, Giles A. Tumor radiation response enhancement by acoustical stimulation of the vasculature. Proceedings of the National Academy of Sciences of the United States of America. 2012; 109:E2033–E2041. [PubMed: 22778441]

Del Grosso VA, Mader CW. Speed of sound in pure water. J Acoust Soc Am. 1972; 52:1442–1446.

Fry FJ, Barger JE. Acoustical properties of the human skull. J Acoust Soc Am. 1978; 63:1576. [PubMed: 690336]

Greenleaf WJ, Bolander ME, Sarkar G, Goldring MB, Greenleaf JF. Artificial cavitation nuclei significantly enhance acoustically induced cell transfection. Ultrasound in medicine & biology. 1998; 24:587–595. [PubMed: 9651968]

Gyongy M, Coussios CC. Passive cavitation mapping for localization and tracking of bubble dynamics. J Acoust Soc Am. 2010a; 128:EL175–EL180. [PubMed: 20968322]

Gyongy M, Coussios CC. Passive spatial mapping of inertial cavitation during HIFU exposure. IEEE transactions on bio-medical engineering. 2010b; 57:48–56. [PubMed: 19628450]

Haworth KJ, Mast TD, Radhakrishnan K, Burgess MT, Kopechek JA, Huang SL, McPherson DD, Holland CK. Passive imaging with pulsed ultrasound insonations. J Acoust Soc Am. 2012; 132:544–553. [PubMed: 22779500]

Hynynen K, McDannold N, Vykhodtseva N, Jolesz FA. Noninvasive MR imaging-guided focal opening of the blood-brain barrier in rabbits. Radiology. 2001; 220:640–646. [PubMed: 11526261]

Marmottant P, Hilgenfeldt S. Controlled vesicle deformation and lysis by single oscillating bubbles. Nature. 2003; 423:153–156. [PubMed: 12736680]

Martin E, Jeanmonod D, Morel A, Zadicario E, Werner B. High-intensity focused ultrasound for noninvasive functional neurosurgery. Ann Neurol. 2009; 66:858–861. [PubMed: 20033983]

McDannold N, Arvanitis CD, Vykhodtseva N, Livingstone MS. Temporary disruption of the blood-brain barrier by use of ultrasound and microbubbles: safety and efficacy evaluation in rhesus macaques. Cancer research. 2012; 72:3652–3663. [PubMed: 22552291]

McDannold N, Clement GT, Black P, Jolesz F, Hynynen K. Transcranial magnetic resonance imaging-guided focused ultrasound surgery of brain tumors: initial findings in 3 patients. Neurosurgery. 2010; 66:323–332. [PubMed: 20087132]

McDannold N, Vykhodtseva N, Hynynen K. Targeted disruption of the blood-brain barrier with focused ultrasound: association with cavitation activity. Physics in medicine and biology. 2006a; 51:793–807. [PubMed: 16467579]

McDannold NJ, Vykhodtseva NI, Hynynen K. Microbubble contrast agent with focused ultrasound to create brain lesions at low power levels: MR imaging and histologic study in rabbits. Radiology. 2006b; 241:95–106. [PubMed: 16990673]

Meairs S, Alonso A, Hennerici MG. Progress in sonothrombolysis for the treatment of stroke. Stroke; a journal of cerebral circulation. 2012; 43:1706–1710.

Norton SJ, Carr BJ, Witten AJ. Passive imaging of underground acoustic sources. J Acoust Soc Am. 2006; 119:2840–2847.

Norton SJ, Won IJ. Time exposure acoustics. IEEE Trans Geosci Rem Sens. 2000; 38:1337–1343.

O'Reilly MA, Hynynen K. Blood-Brain Barrier: Real-time Feedback-controlled Focused Ultrasound Disruption by Using an Acoustic Emissions-based Controller. Radiology. 2012; 263:96–106. [PubMed: 22332065]

O'Reilly MA, Rahman S, Song J, Lucht B, Hynynen K. Design and construction of a passive receiver array for monitoring transcranial focused ultrasound therapy. IEEE Ultrasonics Symposium Proceedings. 2010:892.

Parsons JE, Cain CA, Abrams GD, Fowlkes JB. Pulsed cavitational ultrasound therapy for controlled tissue homogenization. Ultrasound in medicine & biology. 2006; 32:115. [PubMed: 16364803]

Rooney JA. Shear as a mechanism for sonically induced biological effects. J Acoust Soc Am. 1972; 52:1718–1724. [PubMed: 4641374]

Tung YS, Vlachos F, Choi JJ, Deffieux T, Selert K, Konofagou EE. In vivo transcranial cavitation threshold detection during ultrasound-induced blood-brain barrier opening in mice. Physics in medicine and biology. 2010; 55:6141–6155. [PubMed: 20876972]

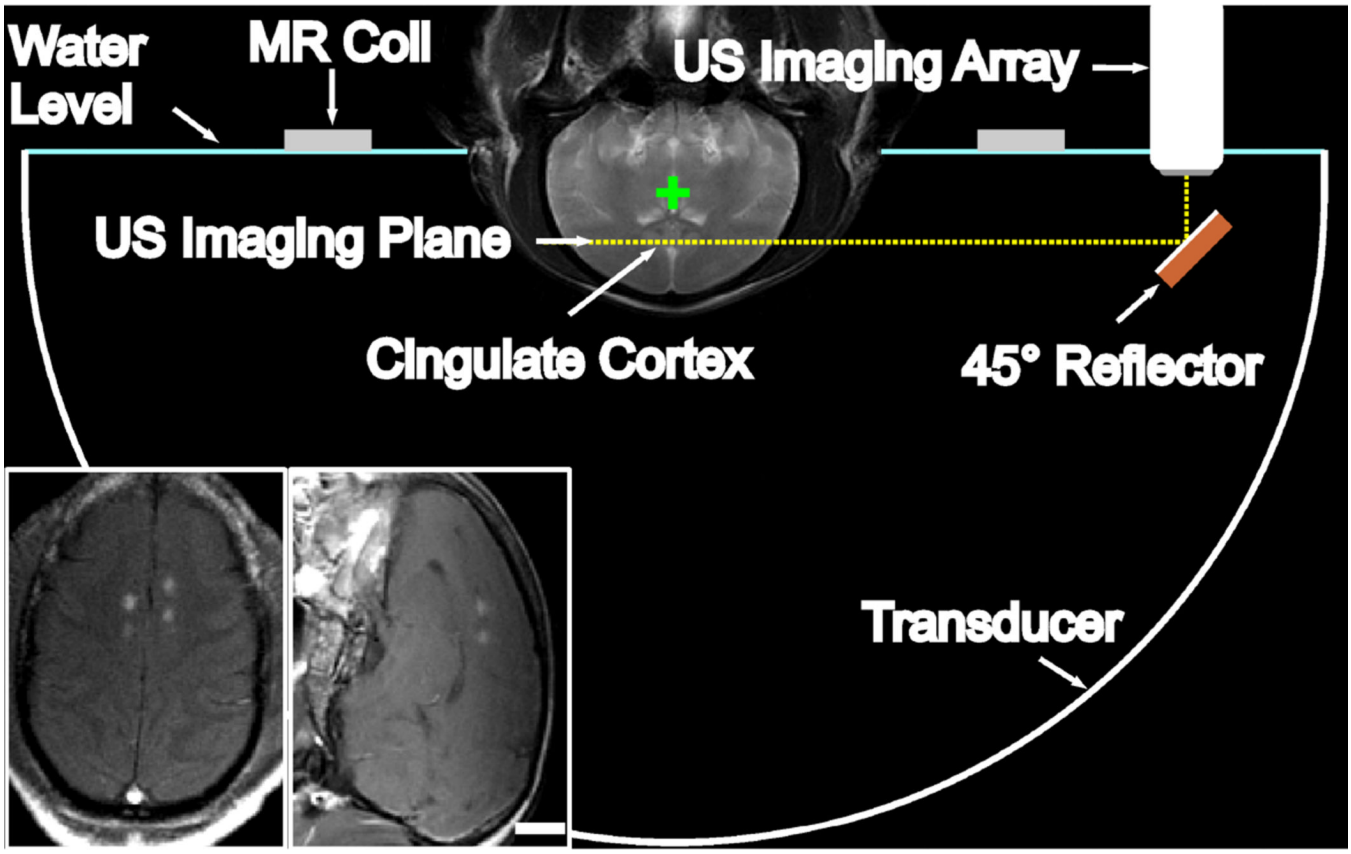

Fig 1.

Pre- and post-sonication MRI of a macaque within the MRgFUS device in the presence of the ultrasound imaging system. A coronal T2-weighted MR image used for treatment planning is shown (pre-sonication). It has been annotated to show the location of the 30 cm diameter hemisphere MRgFUS transducer, the ultrasound imaging array that was connected to the research imaging engine, and the MRI surface coil. The annotations were drawn to scale with the location of the head in a typical position. A 45° brass reflector was used to create an axial imaging plane (yellow dotted line). The imaging array was located 13 cm away from FUS geometrical focus, similar to what might be used in a human. Additional acoustic emissions measurements were obtained using two piezoelectric elements placed in front and back of the head (not shown) at the depth of the geometric focus of the FUS transducer (green cross). The focal point was moved to different brain targets without moving the transducer using the phased array for electronic beam steering. **Inset** (post sonication): Axial (left image) and sagittal (right image) contrast-enhanced T1-weighted MR images showing discrete spots with contrast enhancement, reflecting the localized BBB disruption induced by the sonications. The half-intensity beam width of the focal region for this MRgFUS system was 3.0 and 5.8 mm in the lateral and axial directions respectively. Bar: 1 cm.

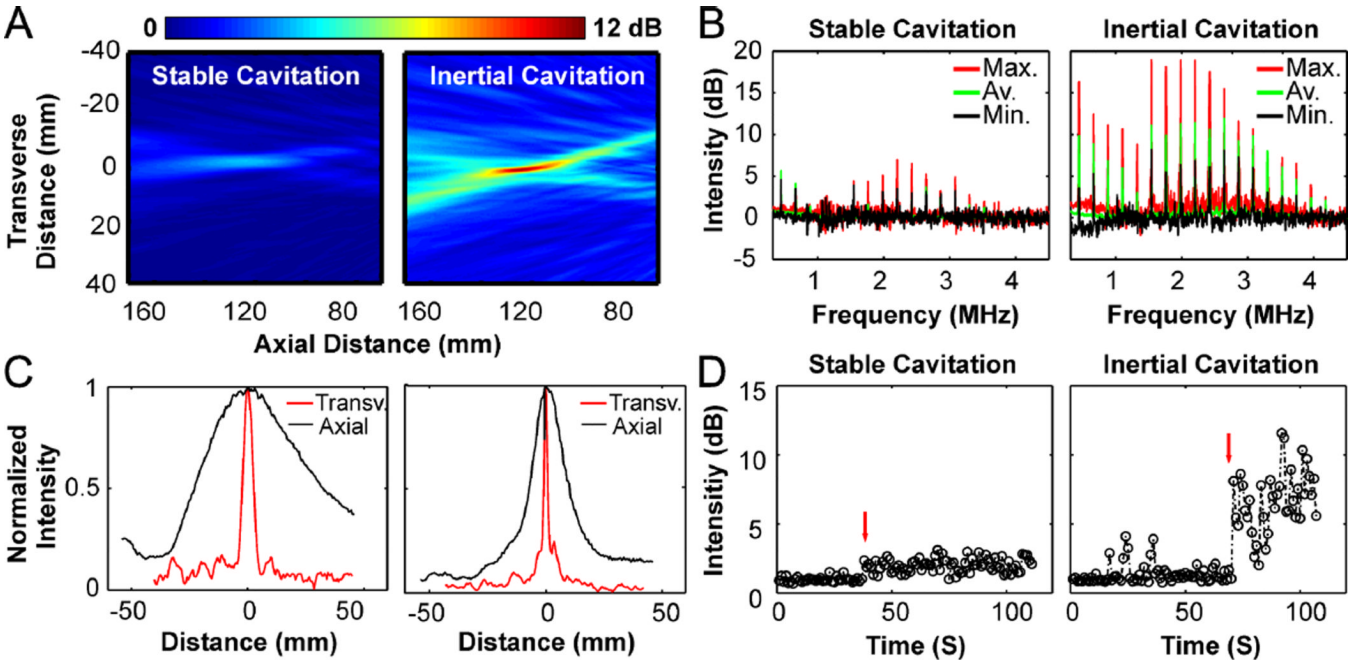

Fig 2.

Representative data obtained transcranially from two different animals with the passive US imaging system during sonications in the cingulate cortex. **(A)** Average cavitation maps of all of the bursts applied during the highest power sonication applied at two targets in one monkey. The images were normalized to data obtained during sonications with identical settings without microbubbles. They are scaled equally and are expressed in dB. The ultrasound imaging array was located to the right of the images **(B)** The corresponding normalized power spectra (NPS) for these sonications are shown for the bursts with the weakest and strongest signals as well as the average over all bursts. From this analysis, we can conclude that the left image in **(A)** was formed by acoustic emissions with harmonic components only (i.e. stable cavitation), and the right image in **(A)** was formed by acoustic emissions with harmonic, ultra-harmonic and broadband components (i.e. inertial cavitation). The frequency axis was normalized to the sonication frequency (0.22 MHz). **(C)** The respective axial and transverse profiles of the maps (right-left and anterior-posterior in transverse and coronal plane respectively in MR coordinates). The FWHM of the activity with stable cavitation was 5 and 55 mm in the transverse and axial directions, respectively. With inertial cavitation, these values were 1.74 and 17 mm. **(D)** The maximum value of the cavitation map as a function of time for stable (left) and inertial (right) cavitation activity. Sonication, imaging, and microbubble injection began simultaneously; the arrow marks the arrival to the microbubbles to the focal region. The spikes prior to this time are presumably from microbubbles remaining in the circulation from a previous sonication.

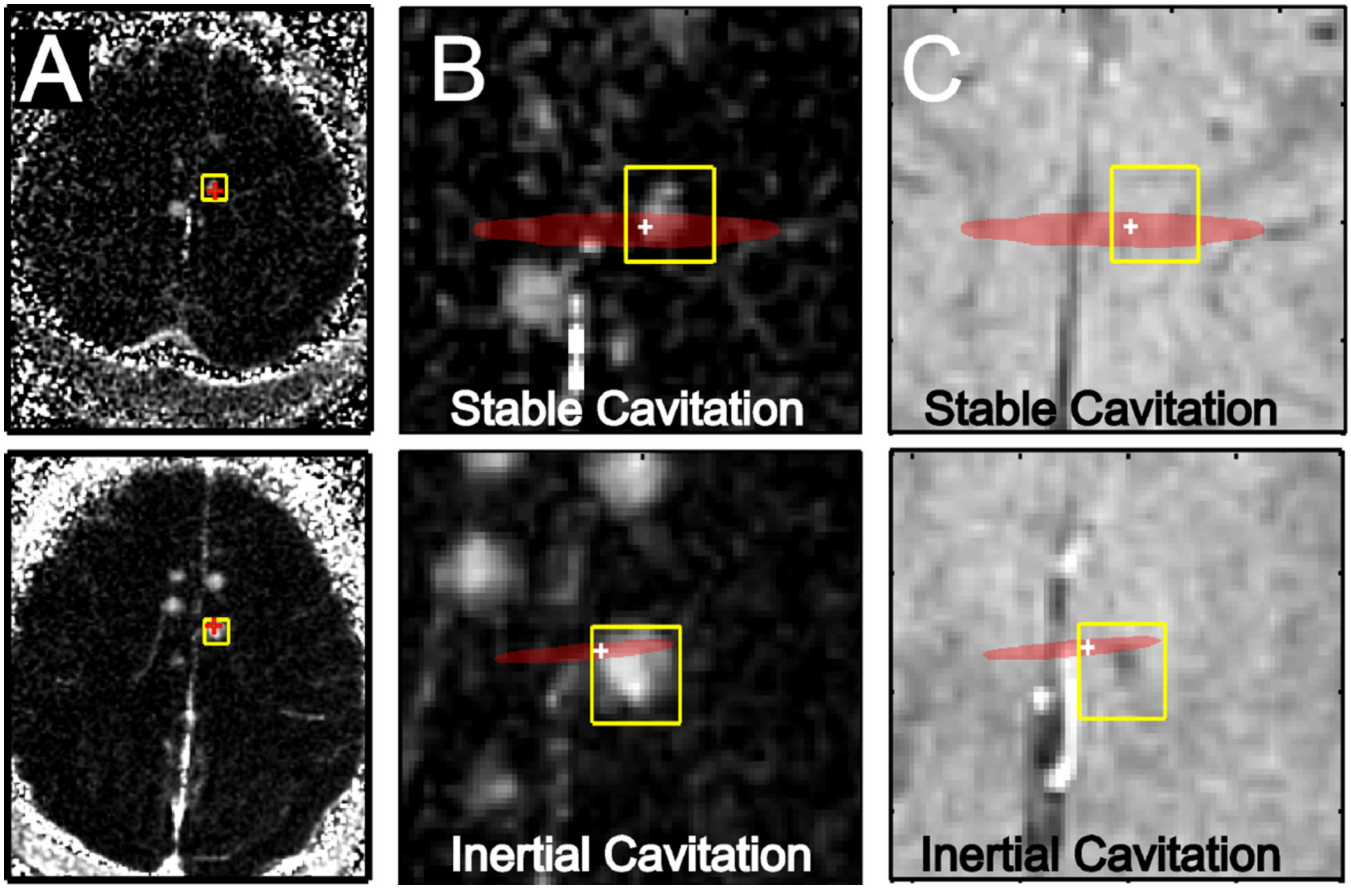

Fig 3.

Fusion of averaged stable and inertial passive cavitation maps from the two sonications shown in Fig. 2 **(A)** Images showing signal enhancement in T1-weighted MRI after Gd-DTPA injection. Top: Data from the sonication with stable cavitation. Bottom: Data from the sonication with inertial cavitation. **(B)** A region showing the pixels in the cavitation maps within 95% of the maximum value is shown; it overlapped with the contrast enhancement. The pixel with the maximum cavitation activity is noted with a "+". The enhancement from other targets sonicated in the same session is visible. **(C)** T2*-weighted images, which become hypointense at the focal spot when petechiae are induced by inertial cavitation. A small hypointense spot was observed (arrow) after the sonication with broadband emission, a signature for inertial cavitation. The ultrasound imaging array was located to the right of the images.

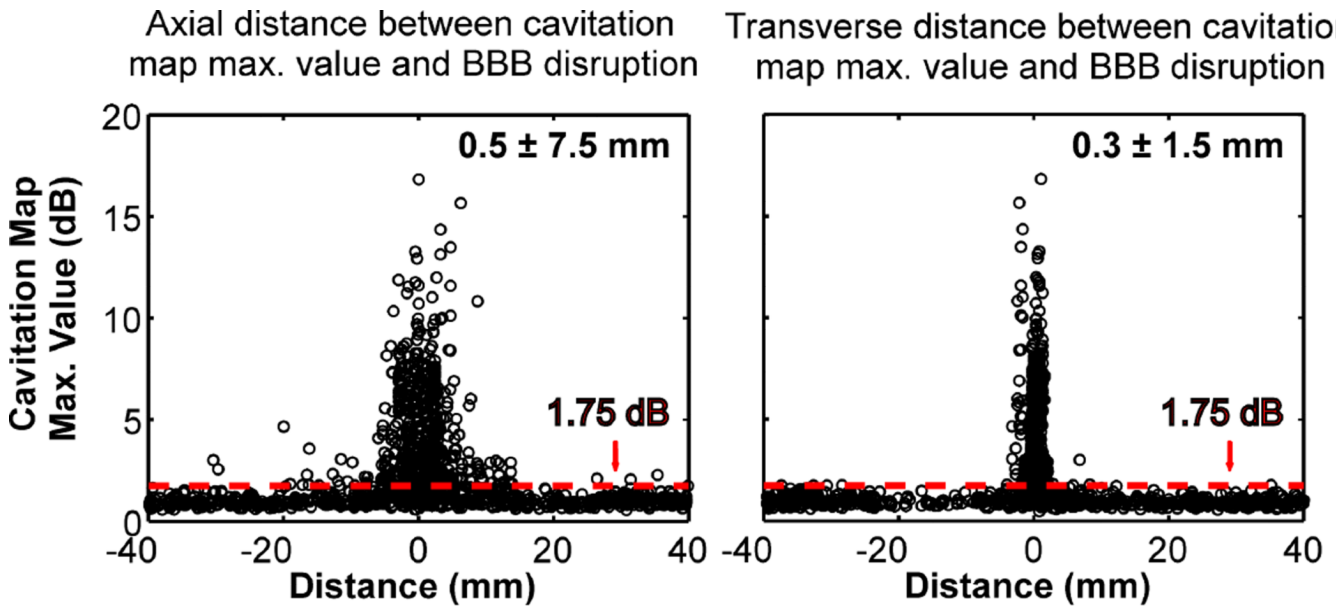

Fig 4.

Evaluation of the colocalization of the cavitation activity and the resulting BBB disruption. Plot of the strength of the cavitation maps at the pixel with the greatest activity as a function of the distance between this pixel and the center of MRI contrast enhancement (left: distance in the axial direction in the ultrasound images; right: transverse direction). Data are shown from the individual cavitation maps obtained for each burst for all of the targets examined (N=1475). When the cavitation activity was greater than 1.75 dB the localization was reliable. The median distance between the maximum cavitation activity and the location of the BBB disruption was within the range of theoretical estimates for the resolution of the cavitation maps (7.5 and 0.5 mm in the axial and transverse directions, respectively).

Table 1

Parameters used for MR imaging

Sequence	Use	TR (ms)	TE (ms)	TI (ms)	Flip Angle	FOV (cm)	Matrix Size	Slice Thickness (mm)	NEX	ETL	Bandwidth (kHz)
3D T1-weighted GE + inversion recovery preparation	Registration between US/MR imaging (fiducials); Treatment planning (monkey)	5.3	2	600	10°	12	128×128	2	0.5	N/A	±15.6
3D T2*-weighted GE	Detection of vascular damage (petechiae)	33.3	19	N/A	15°	12	256×256	1	1	N/A	±15.6
2D T1-weighted FSE (±Gd-DTPA)	Detection of BBB disruption	500	14	N/A	90°	12	256×256	3	4	4	±15.6
2D T2-weighted FSE	Anatomy, detection of edema	4500	85	N/A	90°	12	256×256	3	2	8	±15.6

GE: Gradient Echo; FSE: Fast Spin Echo; TR: Repetition Time; TE: Echo Time; TI: Inversion Time; FOV: Field of View; ETL: Echo Train Length; NEX: Number of Excitations (Averages)

Table 2

Acoustic power level used (inW) at the different targets in each animal.

Monkey	Sex,Weight	Session	Cingulate Cortex			
			Left Posterior (#1)	Right Posterior (#2)	Left Anterior (#3)	Right Anterior (#4)
1	F, 6 kg	1	0.5 – 0.75	0.75 – 1.0	1.0	1.2 – 1.3
		2	0.75 – 1.0	1.0 – 1.2	1.0 – 1.3	1.15 – 1.3
2	M, 6 kg	1	0.5 – 1.0	1.0	1.2 – 1.5	1.55 – 1.6
		2	1.4 – 1.5	1.5 – 2.0	1.7 – 2.2	2.2
3	M, 4.5 kg	1	0.5 – 1.5	1.0 – 1.5	1.0 – 1.5*	1.0 – 1.5

*Acoustic emissions data excluded from one sonication due to animal movement during the sonications.